Lattice QCD study of $\pi\Sigma$–$\bar{K}N$ scattering and the $\Lambda(1405)$ resonance

John Bulava,[1] Bárbara Cid-Mora,[2] Andrew D. Hanlon,[3] Ben Hörz,[4] Daniel Mohler,[5,2] Colin Morningstar,[6] Joseph Moscoso,[7] Amy Nicholson,[7] Fernando Romero-López,[8] Sarah Skinner,[6] and André Walker-Loud[9]

(for the Baryon Scattering (BaSc) Collaboration)

[1] *Deutsches Elektronen-Synchrotron (DESY), Platanenallee 6, 15738 Zeuthen, Germany*
[2] *GSI Helmholtz Centre for Heavy Ion Research, Darmstadt, Germany*
[3] *Physics Department, Brookhaven National Laboratory, Upton, New York 11973, USA*
[4] *Intel Deutschland GmbH, Dornacher Str. 1, 85622 Feldkirchen, Germany*
[5] *Institut für Kernphysik, Technische Universität Darmstadt, Schlossgartenstrasse 2, 64289 Darmstadt, Germany*
[6] *Department of Physics, Carnegie Mellon University, Pittsburgh, Pennsylvania 15213, USA*
[7] *Department of Physics and Astronomy, University of North Carolina, Chapel Hill, NC 27516-3255, USA*
[8] *Center for Theoretical Physics, Massachusetts Institute of Technology, Cambridge, MA 02139, USA*
[9] *Nuclear Science Division, Lawrence Berkeley National Laboratory, Berkeley, CA 94720, USA*

(Dated: July 26, 2023)

A lattice QCD computation of the coupled channel $\pi\Sigma$–$\bar{K}N$ scattering amplitudes in the $\Lambda(1405)$ region is detailed. Results are obtained using a single ensemble of gauge field configurations with $N_f = 2+1$ dynamical quark flavors and $m_\pi \approx 200$ MeV and $m_K \approx 487$ MeV. Hermitian correlation matrices using both single baryon and meson-baryon interpolating operators for a variety of different total momenta and irreducible representations are used. Several parametrizations of the two-channel scattering K-matrix are utilized to obtain the scattering amplitudes from the finite-volume spectrum. The amplitudes, continued to the complex energy plane, exhibit a virtual bound state below the $\pi\Sigma$ threshold and a resonance pole just below the $\bar{K}N$ threshold.

I. INTRODUCTION

In meson-baryon scattering with strangeness $S = -1$ and isospin $I = 0$, the Particle Data Group[1] currently recognizes a 4-star resonance of spin $J = 1/2$, negative parity, and mass near 1405 MeV, known as the $\Lambda(1405)$. A possible nearby resonance of the same quantum numbers, referred to as the $\Lambda(1380)$, is listed with only 2-star status. The issue of whether or not this lower-lying resonance actually exists is of great interest in hadron physics. In fact, Ref. [1] includes an entire Section 83 dedicated to discussing the pole structure of the $\Lambda(1405)$ region.

The $\Lambda(1405)$ resonance first appeared when low-energy K^-p amplitudes measured in bubble chamber experiments [2, 3] implied a resonance in the $\pi^-\Sigma^+$ spectrum just below the K^-p threshold. For a review of experimental progress in this system, see Refs. [4, 5]. Recent precise measurements of the energy shift and width of kaonic hydrogen by the SIDDHARTHA collaboration at DAΦNE [6] have led to improved determinations of the K^-p scattering length, as discussed in Ref. [7]. The CLAS collaboration at JLab investigated the angular dependence of the reaction $\gamma+p \to K^+ + \Sigma + \pi$, determining the line shapes [8] and confirming [9] that the $\Lambda(1405)$ resonance has spin and parity $J^P = 1/2^-$. Using a chiral unitary framework, Refs. [10, 11] found the CLAS data to be consistent with a two-pole picture. Recent studies by the BGOOD collaboration [12] and the ALICE collaboration [13] also support a two-pole scenario. A preliminary analysis by the GlueX collaboration [14] favors two isoscalar poles, while J-PARC [15] claim a single pole describes their data. An overarching analysis in Ref. [16] favors a single resonance, but does not rule out the two-pole picture.

Scattering in the $\Lambda(1405)$ region also poses a challenge for theory. Accommodating the low mass and quantum numbers of the $\Lambda(1405)$ resonance in constituent quark models, such as Ref. [17], is problematic. The presence of two poles in this region was first suggested in Ref. [18]. Nearly all approaches based on $SU(3)$ chiral effective theory, which are reviewed in Refs. [19, 20], predict the presence of two poles in the scattering matrix analytically continued to complex center-of-mass energies, but disagree about the position of the lower pole. See Refs. [21–28] for some other recent theoretical studies of the $\Lambda(1405)$ resonances.

The above considerations suggest that a first-principles investigation of the pole structure in the region of the $\Lambda(1405)$ resonance is warranted. All previous lattice QCD computations of the $\Lambda(1405)$ have not computed scattering amplitudes and instead aimed only to isolate the lowest finite-volume energy eigenstate using single-baryon three-quark interpolating fields [29–37]. However, the use of local single-hadron interpolating fields alone is insufficient to correctly determine the finite-volume spectrum above two-hadron thresholds [38–40]. The $\bar{K}N$ scattering length for $I = 0$ has also been computed long ago using the quenched approximation in Ref. [41], but neglecting the mixing with the kinematically-open $\pi\Sigma$ channel and ignoring unitarity violation due to the quenched approximation, which invalidates the relation between the finite-volume spectrum and scattering amplitudes [42]. The $\pi\Sigma$ and $\bar{K}N$ scattering lengths in other (non-singlet) flavor and isospin combinations not directly relevant for the $\Lambda(1405)$ have also been computed

in Refs. [43–45].

A recent study [46] of nucleon-pion scattering in the region of the Δ-resonance demonstrates that current lattice QCD techniques are sufficiently efficacious for studying simple baryon resonances. In this work, we apply these techniques to the isospin $I = 0$ and strangeness $S = -1$ coupled-channel $\pi\Sigma - \bar{K}N$ scattering amplitudes below the $\pi\pi\Lambda$ threshold for the first time. Hermitian correlation matrices using both single baryon and meson-baryon interpolating operators for a variety of different total momenta and irreducible representations are used to obtain the finite-volume stationary-state energies. A set of parametrizations of the scattering amplitudes are then constrained by fits to the finite-volume energy spectrum using a well-known quantization condition. The amplitudes, continued to the complex energy plane, exhibit a virtual bound state below the $\pi\Sigma$ threshold and a resonance pole just below the $\bar{K}N$ threshold, the positions of which vary little with differing fit forms and are broadly consistent with predictions from chiral effective theory. This work constitutes the first coupled-channel scattering study in lattice QCD to include baryons; only coupled-meson systems have been previously studied [40, 47–51]. Highlights of this study were previously presented in Ref. [52]. Further technical details of the investigation are reported here.

This work is organized as follows. The determination of the finite-volume stationary-state energies is presented in Sec. II, including the ensemble details, method of evaluating the correlation functions, and the extraction of the energies. Details on the determinations of the scattering amplitudes are then presented in Sec. III. The quantization condition that relates the amplitudes to the finite-volume spectrum is reviewed, the parametrizations of the K-matrix that we use are described, and the fits using these parametrizations and the quantization condition are detailed. Analytic continuation of the scattering transition amplitudes to complex energies is then used to determine nearby S-matrix poles.

II. SPECTRUM COMPUTATION

This section describes the determination of the finite-volume stationary-state energies. The procedure used follows an approach similar to Ref. [46], but for the convenience of the reader, some of the main details of the method are repeated here, along with a summary of our results.

A. Ensemble details

A single ensemble of QCD gauge configurations is employed with dynamical mass-degenerate u- and d-quarks which are heavier than physical, and an s-quark lighter than physical, resulting in a pion mass $m_\pi \approx 200$ MeV and a kaon mass $m_{\rm K} \approx 487$ MeV, which differ slightly from their physical values $m_\pi^{\rm phys} \approx 140$ MeV and $m_{\rm K}^{\rm phys} \approx 495$ MeV. The key properties of this so-called D200 ensemble are summarized in Table I. The configurations were generated by the Coordinated Lattice Simulations (CLS) consortium [53] using the tree-level improved Lüscher-Weisz gauge action [54] and a non-perturbatively $O(a)$-improved Wilson fermion action [55]. Open temporal boundary conditions [56] were employed to reduce the autocorrelation of the global topological charge, but this then requires that all interpolating fields are sufficiently far from the boundaries, limiting the maximum temporal separation in correlation functions to $t_{\rm max} = 25a$. The algorithm used to generate the D200 ensemble is described in Ref. [53]. Low-lying eigenvalues of the Dirac matrix of either the light quark doublet or the strange quark can cause instabilities in the Hybrid Monte Carlo (HMC) or Rational Hybrid Monte Carlo (RHMC) algorithm[57] for generating the gauge fields, an issue which is sufficiently ameliorated for the D200 ensemble [58] by light- and strange-quark re-weighting [59]. Re-weighting factors must be included in the analysis to convert the simulated action to the desired one, and we use the factors computed in [60]. The lattice spacing is determined in Ref. [61] and updated in Ref. [62].

TABLE I. Parameters of the D200 ensemble [53]. The spatial extent L and temporal extent T of the lattice are given, as well as the masses $m_\pi, m_{\rm K}$ of the pion and kaon, respectively, in units of the lattice spacing a.

a[fm]	$(L/a)^3 \times T/a$	am_π	$am_{\rm K}$
0.0633(4)(6)	$64^3 \times 128$	0.06533(25)	0.15602(16)

Correlation function evaluations are separated by four molecular dynamics units (MDU's) in the Monte Carlo Markov chain. Our study of autocorrelations is summarized in Fig. 1. The top panel of this figure shows how the variance in the pion mass determination increases as the original measurements are rebinned. The variance initially increases with increasing $N_{\rm bin}$, until little difference is observed in going from $N_{\rm bin} = 10$ to $N_{\rm bin} = 20$. The bottom panel displaying the correlated χ^2/dof shows the expected reduction due to the larger variance with increasing $N_{\rm bin}$. For $N_{\rm bin} > 15$ the correlated-χ^2 of the pion fit increases again, likely due to degrading estimates of the covariance matrix. Fits to determine the nucleon mass were also found to have similar behavior. Hence, in this work, all primary quantities are first binned by averaging over $N_{\rm bin} = 10$ consecutive gauge configurations.

B. Correlator determinations

Our operator construction is described in Ref. [63] and our method of evaluating the temporal correlators is detailed in Ref. [64]. We use multi-hadron operators comprised of individual constituent hadrons, each corresponding to a definite momentum. The single hadron op-

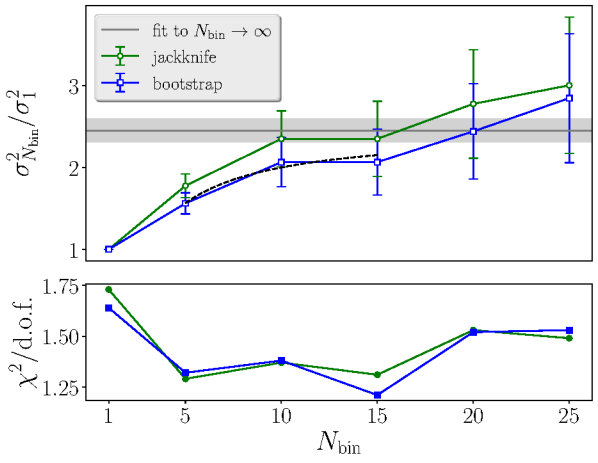

FIG. 1. (Top) Ratios of variances for fits to determine am_π for various bin sizes $N_{\rm bin}$ over the variance for $N_{\rm bin} = 1$. Both the jackknife and bootstrap procedure are employed. (Bottom) The correlated-χ^2 for two-exponential fits to the pion correlator over a range in temporal separation $[t_{\rm min}, t_{\rm max}] = [10a, 25a]$ for various rebinning factors. Jackknife and bootstrap ($N_B = 800$) resampling methods are compared.

erators are appropriate assemblages of gauge-covariantly smeared quark fields. The quark fields are smeared using the Laplacian Heaviside (LapH) procedure described in Ref. [65]. This smearing employs a projection onto the subspace spanned by the $N_{\rm ev}$ lowest eigenmodes of the gauge-covariant three-dimensional Laplacian operator, expressed in terms of link variables which are stout smeared [66]. The stout smearing parameters are denoted by (ρ, n_ρ). The multi-hadron operators used in this study are presented in the tables of Appendix A.

Evaluating the temporal correlations of our operator sets requires time-slice to time-slice quark propagators, which we estimate using the stochastic LapH method [64]. This method employs variance reduction using noise dilution projectors. Each projector is a product of time ('T'), spin ('S'), and Laplacian eigenvector index ('L') projectors. For each, the different schemes used are denoted by 'F' for full dilution and 'In' for some number n of uniformly interlaced projectors. Different dilution schemes are used for fixed-time quark lines, denoted 'fix', which propagate from the source time-slice to the sink time-slice, and relative-time lines ('rel') which start and end at the same time. In this work, the relative-time quark lines are only used at the sink time, while the fixed-time lines are used for quark propagation starting and ending at the source time. The smearing parameters and the dilution schemes used are specified in Table II. Source times $t_0 = 35a, 64a$ are used for correlations going forwards in time, and $t_0 = 64a, 92a$ are used for correlations going backwards in time. Correlators for the different rows of the little group irreducible representations (irreps) and for total momenta in all directions of the same magnitudes squared are averaged to increase statistics. An advantageous feature of the stochastic LapH method is source-sink factorization of the correlators which greatly facilitates the evaluation of large Hermitian correlation matrices containing single-baryon, $\pi\Sigma$, and $\bar{K}N$ interpolating operators via optimized tensor contractions [67].

TABLE II. Parameters of the stochastic LapH implementation used to compute temporal correlators in this work. The stout smearing parameters for the spatial links in the gauge-covariant Laplace operator are (ρ, n_ρ), and $N_{\rm ev}$ denotes the dimension of the LapH subspace. Notation used to specify the dilution scheme for each line type is explained in the text.

(ρ, n_ρ)	$N_{\rm ev}$	Noise dilution	
(0.1, 36)	448	$(\text{TF, SF, LI16})_{\rm fix}$	$(\text{TI8, SF, LI16})_{\rm rel}$

C. Finite-volume energies

Once Markov-chain Monte Carlo estimates of the correlation functions are obtained, the determination of finite-volume energies can then be achieved. Single-hadron energies corresponding to the lowest-lying mesons and baryons are obtained from the single diagonal correlators of the relevant single-hadron operators. For the spectra of stationary-state energies, the entire correlation matrices involving all operators in a given symmetry channel must be used. The symmetry channels are labeled by their total isospin I, total strangeness S, and the irreducible representation (irrep) $\Lambda(\boldsymbol{d}^2)$ of the little group for the total momentum squared $\boldsymbol{P}^2 = (2\pi/L)^2\boldsymbol{d}^2$, where $\boldsymbol{d}$ is a three-vector of integers and L is the extent of the L^3 spatial lattice. Both single-baryon and meson-baryon operators are used in the correlation matrices evaluated in this work. The correlator matrices are then diagonalized, as described in Ref. [46] and summarized below, using solutions of a judiciously-formed generalized eigenvalue problem (GEVP). Each finite-volume stationary-state energy is then extracted from fits to each of the resulting diagonal correlators.

Energies are determined from correlated-χ^2 fits to both single- and two-exponential fit forms over various fit ranges $[t_{\rm min}, t_{\rm max}]$, which are additionally compared to a "geometric-exp series" form [46]

$$C(t) = \frac{A\mathrm{e}^{-Et}}{1 - B\mathrm{e}^{-Mt}}, \tag{1}$$

which consists of four free parameters. We also explored a "multi-exponential" variant of the geometric-exp series, with the replacement $Be^{-Mt} \to \sum_n B_n e^{-M_n t}$. The optimal fit for an energy determination is chosen so that the statistical error on the energy encompasses any variation between fit forms and is reasonably insensitive to $t_{\rm min}$. However, the open temporal boundary conditions limit

TABLE III. A summary of various hadron masses and decay constants (with normalization $f_\pi^{\rm phys} \approx 130$ MeV) for the CLS D200 gauge ensemble used in this work. The η mass is taken from Ref. [68], and the pion and kaon decay constants are taken from Ref. [69]. All other masses are determined in Fig. 2.

am_π	0.06533(25)	af_π	0.04226(13)
am_K	0.15602(16)	af_K	0.04910(11)
am_η	0.1768(22)	am_Λ	0.3634(14)
am_N	0.3143(37)	am_Σ	0.3830(19)

the range of the correlation functions. For our choice of source time-slices this results in $t_{\rm max} = 25a$. At the same time, the energy gap between the desired ground state and unwanted excited states decreases as the pion mass is lowered to the physical point. The limited time range and small energy gap often result in an insufficient description of the data using the single-exponential fit form. The two-exponential form and the 'geometric-exp' form, however, do result in suitable descriptions of the data and provide consistent energy determinations.

Determinations of the pion, kaon, nucleon, Σ, and Λ, masses are shown in Fig. 2 and their values are presented in Table III. This table also includes the η mass, as well as the pion and kaon decay constants. The hadrons listed in this table are all stable in the absence of electroweak interactions and in the isospin limit with $m_u = m_d$.

Before extracting a spectrum of stationary-state energies, the correlation matrix $C_{ij}(t)$ in a given symmetry channel is transformed[70] to a diagonal form $D_{ab}(t)$ using the eigenvectors $v_n(t_0, t_{\rm d})$ of the GEVP

$$C(t_{\rm d})v_n(t_0, t_{\rm d}) = \lambda_n(t_0, t_{\rm d})\; C(t_0)\; v_n(t_0, t_{\rm d}), \qquad (2)$$

where t_0 is referred to as the *metric time*, $t_{\rm d}$ is called the *diagonalization time*, and λ_n denote the eigenvalues. The diagonal elements of the resulting matrix $D(t)$ are referred to here as the *rotated* correlators. In this work, two different ways of carrying out the above transformation are used.

In the simplest approach, known as a *single pivot*, a single judicious choice of t_0 and $t_{\rm d}$ is used to transform the correlation matrix for all times t. We typically choose t_0 to be about half of $t_{\rm d}$ to minimize contamination from higher-lying states [71, 72] and choose $t_{\rm d}$ as small as possible to minimize statistical errors but ensuring that the rotated correlation matrix remains diagonal for all $t > t_{\rm d}$ within the statistical precision of the calculations. The eigenvectors v_n utilized are computed using the mean values of the correlation matrix. In this approach, it is important to check insensitivity of the final spectrum results to a reasonable range of $(t_0, t_{\rm d})$ choices.

In the second approach, known as a *rolling pivot*, a single value of t_0 is used, but $t_{\rm d} = t$ is used for rotating the correlation matrix at time t. In other words, the correlation matrix is separately rotated at every time, keeping the metric time fixed. The eigenvectors employed for each time are determined using the mean values of the correlators. This procedure is much more complicated than the single pivot as the order of the eigenvectors with changing time must be carefully considered. The simplest method of ordering the eigenvectors according to their eigenvalues at time t can lead to diagonal correlators which tend asymptotically towards different stationary-state decay rates for different times t. Hence, some method of eigenvector "pinning" is needed so that a given diagonal correlator is always tending towards the same stationary-state behavior. Diagonalizations at larger times can lead to increased statistical errors, but this method ensures the correlation matrix remains diagonal at all times.

To check that uncertainties determined in the rolling pivot are not underestimated, a variant of the second approach is also used in which the variance in the diagonalized correlators include uncertainties from the GEVP. Instead of using the same eigenvectors from the mean values of the correlators when bootstrapping, the eigenvectors themselves are re-evaluated using the bootstrap resamplings of the correlation matrix.

Fig. 3 shows center-of-mass frame energy determinations in four symmetry channels using the above different approaches. Two different choices of $t_{\rm d}$ in the single pivot method are also shown. The same fitting strategy to extract the energies from the diagonalized correlators was used as for the single hadron energies. One sees that the simplest single-pivot method produces nearly identical results to the other two more complicated methods as long as $(t_0, t_{\rm d})$ are chosen appropriately. Given this stability of the results, our final results used the single-pivot method with $t_0 = 4a$ and $t_{\rm d} = 16a$.

In addition to using the one-exponential, two-exponential, and geometric-exp series fit forms to directly determine the lab-frame stationary-state energies from the diagonal elements of the rotated correlation matrix, a fourth method, already used in Ref. [73], is also used to determine the energies. After forming the rotated correlators $D_n(t)$, the following ratio of correlators is taken

$$R_n(t) = \frac{D_n(t)}{C_A(\boldsymbol{d}_A^2, t)\, C_B(\boldsymbol{d}_B^2, t)}, \qquad (3)$$

where (A, B) is either (π, Σ) or $(\bar{K}, N)$, with $\boldsymbol{d}_A^2$ and $\boldsymbol{d}_B^2$ chosen so that

$$E_n^{\text{non. int.}} = \sqrt{m_A^2 + \left(\frac{2\pi \boldsymbol{d}_A}{L}\right)^2} + \sqrt{m_B^2 + \left(\frac{2\pi \boldsymbol{d}_B}{L}\right)^2} \qquad (4)$$

corresponds to a non-interacting energy sum close to the energy expected for the stationary state. The ratio $R_n(t)$ is then fit to a one-exponential ansatz to determine the energy interaction shift $a\Delta E_n$, from which the lab-frame energy can be reconstructed $aE_n^{\rm lab} = a\Delta E_n + aE_n^{\rm non.int.}$. This method hopes to take advantage of noise cancellation in the ratio of correlators to more precisely determine the interaction shifts. Due to the presence of both $\pi\Sigma$

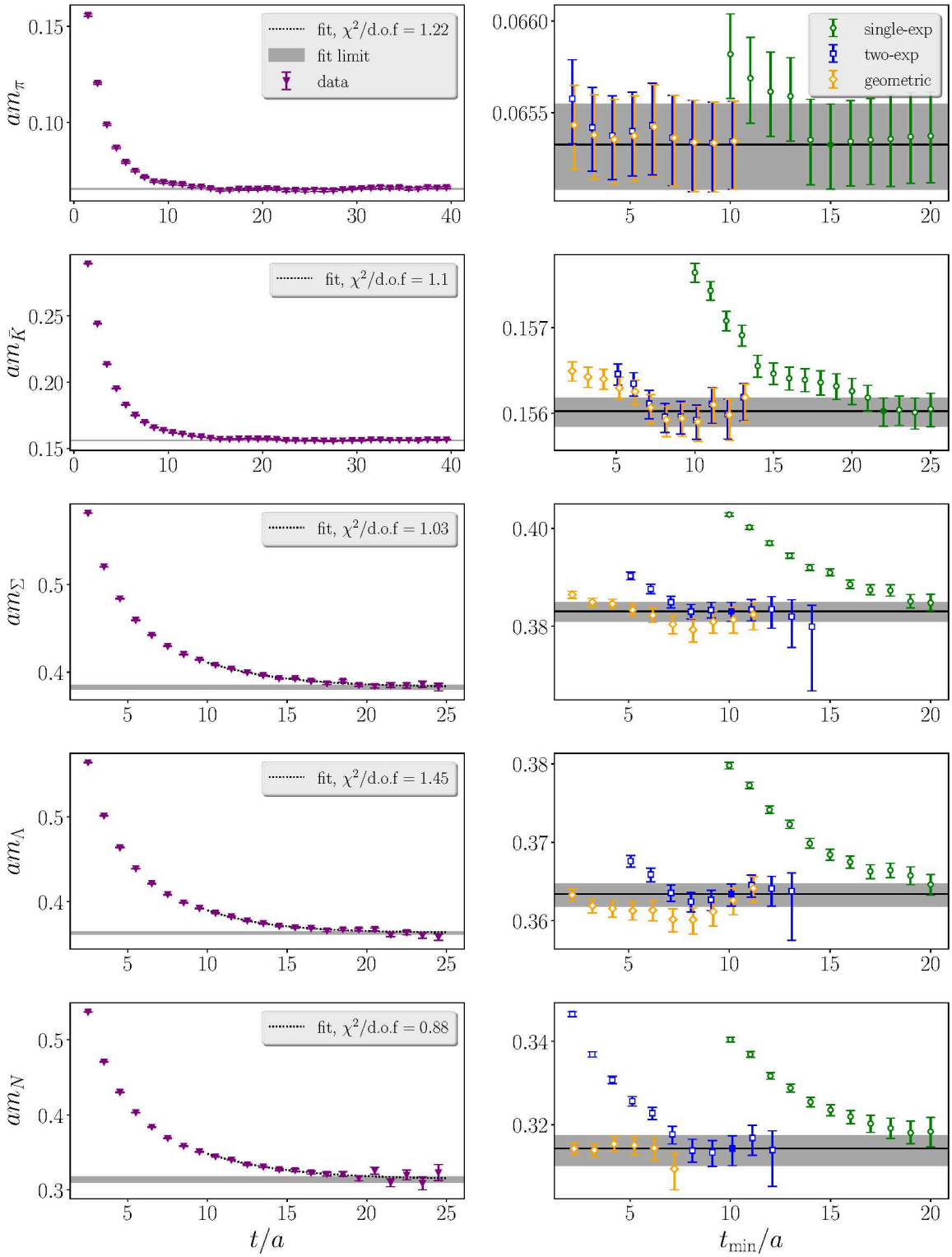

FIG. 2. Determination of single-hadron masses. Each row corresponds to a particular hadron denoted by the label on the vertical axis. The left panel shows the effective energy $\ln(C(t)/C(t+a))$ with two-exponential fits overlayed (dashed lines), except for the pion and kaon for which a single-exponential fit is used. The horizontal band corresponds to the quoted mass and statistical error. The right panel compares different fit forms and different $t_{\rm min}$ choices for fixed $t_{\rm max} = 35a$ for the pion and kaon and $t_{\rm max} = 25a$ for the other hadrons, with the chosen fit denoted by the horizontal band.

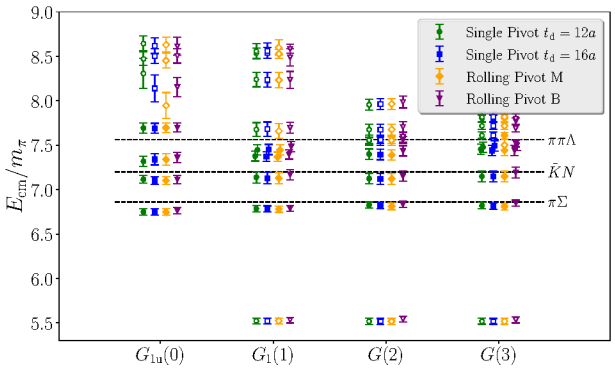

FIG. 3. Stability of the finite-volume spectra under variation of the correlation matrix rotation method using the GEVP for four different symmetry sectors. The metric time is set to $t_0 = 4a$. "Rolling Pivot M" refers to the second approach that uses eigenvectors determined using the mean values of the correlation matrix, and "Rolling Pivot B" refers to the bootstrapped variant of the rolling pivot.

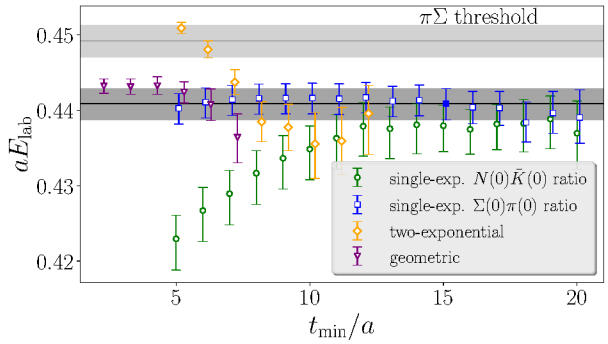

FIG. 4. Determination of the finite-volume stationary-state energy corresponding to the lowest level of the $G_{1u}(0)$ irrep. Each point shows the lab-frame energy from a particular fit using temporal range $t_{\rm min}$, shown on the horizontal axis, to $t_{\rm max} = 25a$. Four different fit methods are shown: two-exponential and geometric-exp fits to the rotated correlator, and single-exponential fits to the ratio of the rotated correlator over the product of single-hadron correlators for either $\bar{K}(0)N(0)$ or $\pi(0)\Sigma(0)$. The dark horizontal band and filled symbol denote the final chosen fit selected as described in the text.

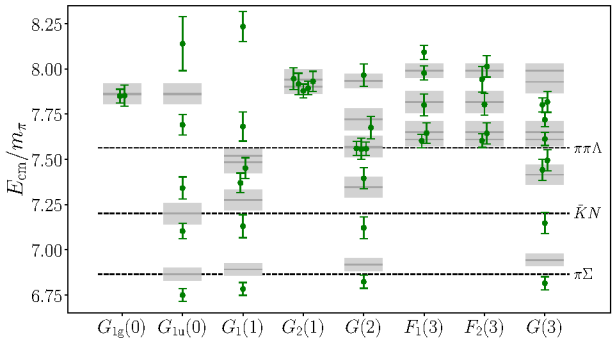

FIG. 5. Finite-volume stationary-state energy spectrum, shown as green points, in the center-of-mass frame for total isospin $I = 0$, strangeness $S = -1$, and various symmetry channels indicated along the horizontal axis. The gray bands show the locations of energy sums for non-interacting two-particle combinations. Various two and three particle thresholds are shown as dashed horizontal lines. Energies are shown as ratios over the pion mass m_π.

and $\bar{K}N$ states, there are often nearby non-interacting sums of each type. Since the reconstructed lab-frame energy should be independent of which product of non-interacting correlators is used in the denominator, we use both types to check for consistency.

To select a final result for use in determining the scattering amplitudes, several general rules of thumb are employed. First, the selected fit must have a p-value greater than 0.1 and/or χ^2/dof less than 1.5. Agreement of the fit result with those from nearby $t_{\rm min}$ values is also considered. When choosing a final fit, we also look for consistency with the other fit methods. From these considerations, a single-exp ratio fit is often selected, and we require that the final fit is within 2σ of the other ratio fit of the same $t_{\rm min}$. Consistency with the plateau regions of the two-exponential and geometric-exp fits is also required. The final fit is chosen as that with the smallest statistical errors which is also stable between nearby $t_{\rm min}$ values and maintains consistency between methods.

An example energy determination is shown in Fig. 4. The energy determined in this example corresponds to the lowest level of the $G_{1u}(0)$ irrep. Results from four different fit methods are shown: two-exponential and geometric-exp fits to the rotated correlator, and single-exponential fits to the ratio of the rotated correlator over the product of single-hadron correlators for either $\bar{K}(0)N(0)$ or $\pi(0)\Sigma(0)$, the zeroes in parentheses referring to $\boldsymbol{d}^2$ of each hadron. The single-exp ratio fit for $t_{\rm min} = 15a$ is selected as the final estimate. Analogous plots for other levels are given in Appendix B.

A summary of the total isospin $I = 0$ and strangeness $S = -1$ spectrum in the center-of-mass frame for various symmetry channels is presented in Fig. 5. Each center-of-mass energy $E_{\rm cm}$ is obtained from the corresponding lab-frame energy $E_{\rm lab}$ using

$$E_{\rm cm} = \sqrt{E_{\rm lab}^2 - \boldsymbol{P}^2}. \tag{5}$$

The results are compared to the energy sums of non-interacting two-particle combinations.

III. SCATTERING AMPLITUDES

Our determinations of the scattering amplitudes are presented in this section. First, the quantization condition that relates the amplitudes to the finite-volume spectrum is discussed. Then the parametrizations of the K-matrix that we use are described, and fits using these parametrizations and the quantization condition are presented.

A. Quantization condition

In lattice QCD, scattering amplitudes are obtained by solving a quantization condition [74–81] which relates the amplitudes to the finite-volume spectrum of center-of-mass energies $E_{\rm cm}$. Generally, the lowest partial wave amplitudes must be somehow parametrized, then best-fit values of the parameters are determined by matching the finite-volume spectrum produced by the quantization condition to that evaluated in lattice QCD.

The form of the quantization condition used here is given by

$$\det[\widetilde{K}^{-1}(E_{\rm cm}) - B^{\boldsymbol{P}}(E_{\rm cm})] + \mathrm{O}(\mathrm{e}^{-ML}) = 0 \ , \qquad (6)$$

where $\widetilde{K}$ is related to the usual scattering K-matrix as described below, and $B^{\boldsymbol{P}}(E_{\rm cm})$ for a particular total momentum $\boldsymbol{P} = (2\pi/L)\boldsymbol{d}$, with $\boldsymbol{d} \in \mathbb{Z}^3$, is the so-called box matrix, using the notation of Ref. [82]. In Eq. (6), the neglected correction terms are suppressed exponentially with the spatial extent L and some relevant energy scale M, typically the pion mass. Eq. (6) applies only for energies below all thresholds of states containing three or more particles. The determinant can be taken over all unit normalized two-hadron states $|Jm_J\ell Sa\rangle$ specified by total angular momentum J, the projection of J along the z-axis m_J, the orbital angular momentum ℓ, the total intrinsic spin S, and particle species a. Here, $a = 0, 1$, where species channel 0 is $\pi\Sigma$ and species channel 1 is $\bar{K}N$, and total spin $S = 1/2$ is fixed, and therefore, need not be explicitly indicated.

The box matrix $\langle J'm'_J\ell'S'a'|\ B^{\boldsymbol{P}}(E_{\rm cm})\ |Jm_J\ell Sa\rangle$ encodes the effects of inserting the partial waves into the cubic box so as to maintain the periodic boundary conditions. This matrix is diagonal in the indices corresponding to total intrinsic spin and particle species, but not to any of the other indices. In particular, states of different total angular momentum can mix. One can show that, under any symmetry transformation Q of the cubic box which is an element of the little group of $\boldsymbol{P}$, the box matrix transforms as $QB^{\boldsymbol{P}}Q^\dagger = B^{\boldsymbol{P}}$. This implies that the box matrix can be block diagonalized by projecting onto the superpositions of states that transform according to the irreps of the little group. The $\widetilde{K}$ matrix similarly block diagonalizes in such a basis, except for the total intrinsic spin and particle species indices. Hence, the determinant in Eq. (6) can be dealt with separately block by block. A particular block can be denoted by the finite-volume irrep $\Lambda(\boldsymbol{d}^2)$ and a row of this irrep λ. Since the spectrum is independent of the row λ, this index is henceforth omitted. For a particular block, the block-diagonalized box-matrix is denoted $B^{\Lambda(\boldsymbol{d}^2)}_{J'\ell' n';J\ell n}$, where n, n' are irrep occurrence numbers. The expressions for all elements of $B^{\Lambda}(\boldsymbol{d}^2)$ relevant for this work are given in Ref. [82]. After transforming to the block diagonal matrix, the $\widetilde{K}$ matrix has the form given by Eq. (35) in Ref. [82]. A truncation $\ell \le \ell_{\rm max}$ in each block then makes the determinant condition manageable.

We use the same definition of the K-matrix as described in Ref. [82]. This matrix is real and symmetric and diagonal in total angular momentum and its projection:

$$\langle J'm'_J\ell'S'a'|K|Jm_J\ell Sa\rangle = \delta_{J'J}\delta_{m'_Jm_J}K^{(J)}_{\ell'S'a';\ell Sa}(E_{\rm cm}). \qquad (7)$$

The matrix $\widetilde{K}$ here is defined by

$$\widetilde{K}^{(J)-1}_{\ell'S'a';\ \ell Sa}(E_{\rm cm}) = k_{a'}^{\ell'+\frac{1}{2}}\ K^{(J)-1}_{\ell'S'a';\ \ell Sa}(E_{\rm cm})\ k_a^{\ell+\frac{1}{2}}, \quad (8)$$

where

$$k_0^2 \ = \ k^2_{\pi\Sigma} = \frac{1}{4E^2_{\rm cm}}\lambda_K(E^2_{\rm cm}, m^2_\pi, m^2_\Sigma), \qquad (9)$$

$$k_1^2 \ = \ k^2_{\bar{K}N} = \frac{1}{4E^2_{\rm cm}}\lambda_K(E^2_{\rm cm}, m^2_{\bar{K}}, m^2_{\rm N}), \qquad (10)$$

and λ_K is the Källén function [83]

$$\lambda(x, y, z) = x^2 + y^2 + z^2 - 2xy - 2xz - 2yz. \qquad (11)$$

Note that this definition of $\widetilde{K}$ differs very slightly from that given in Ref. [82], and hence, the box matrix here also is slightly different. Simple factors related to the spatial extent L have been removed here.

In this work, the total intrinsic spin $S = S' = 1/2$ is fixed, so these indices can be omitted. For elastic scattering, $\widetilde{K}$ is diagonal in the orbital angular momentum, so we take $\ell = \ell'$. We restrict our attention to $\ell \le \ell_{\rm max}$ where $\ell_{\rm max} = 0, 1$. Since parity for $\pi\Sigma$ and $\bar{K}N$ states is $P = (-1)^{\ell+1}$, where the product of the intrinsics parities is -1, and we include only $\ell = 0, 1$ waves, we can change notation to remove ℓ in favor of J^P. Thus, we use the notation $\widetilde{K}^{(J^P)}_{a'a}(E_{\rm cm})$ in what follows, with $J^P = 1/2^-$ for $\ell_{\rm max} = 0$ and $J^P = 1/2^-, 1/2^+, 3/2^+$ for $\ell_{\rm max} = 1$.

B. Parametrizations and fits for $\ell_{\rm max} = 0$

For $\ell_{\rm max} = 0$, the finite-volume spectrum shown in Fig. 5 constrains the coupled-channel scattering amplitude via Eq. (6) at center-of-mass energies near the $\pi\Sigma$ and $\bar{K}N$ thresholds. All irreps in Table 1 of Ref. [46] to which the $J^P = 1/2^-$ partial wave contributes are employed.

Four different types of parametrizations of $\widetilde{K}$ are studied here using $\ell_{\rm max} = 0$. In the expressions below, the subscripts i and j denote either of the two scattering channels (channel 0 is $\pi\Sigma$ and channel 1 is $\bar{K}N$), and the quantity

$$\Delta_{\pi\Sigma}(E_{\rm cm}) = \frac{E_{\rm cm}^2 - (m_\pi + m_\Sigma)^2}{(m_\pi + m_\Sigma)^2}, \tag{12}$$

is related to the center-of-mass energy gap above $\pi\Sigma$ threshold. The matrices A, B, $\widehat{A}$, $\widehat{B}$, $\widetilde{A}$, and $\widetilde{B}$ below are real and symmetric. The four forms of parametrizations are as follows:

1. An effective range expansion (ERE) of the form

$$\widetilde{K}_{ij} = \frac{m_\pi}{E_{\rm cm}}\Big(A_{ij} + B_{ij}\Delta_{\pi\Sigma}(E_{\rm cm})\Big). \tag{13}$$

2. A variation of the first parametrization without the factor of $m_\pi/E_{\rm cm}$:

$$\widetilde{K}_{ij} = \widehat{A}_{ij} + \widehat{B}_{ij}\Delta_{\pi\Sigma}(E_{\rm cm}). \tag{14}$$

3. An ERE of $\widetilde{K}^{-1}$ of the form

$$\widetilde{K}_{ij}^{-1} = \frac{E_{\rm cm}}{m_\pi}\left(\widetilde{A}_{ij} + \widetilde{B}_{ij}\Delta_{\pi\Sigma}(E_{\rm cm})\right). \tag{15}$$

4. A Blatt-Biederharn [84] parametrization:

$$\widetilde{K} = C\ F\ C^{-1}, \tag{16}$$

where

$$C = \begin{pmatrix} \cos\epsilon & \sin\epsilon \\ -\sin\epsilon & \cos\epsilon \end{pmatrix}, \tag{17}$$

$$F = \begin{pmatrix} f_0(E_{\rm cm}) & 0 \\ 0 & f_1(E_{\rm cm}) \end{pmatrix}, \tag{18}$$

and

$$f_i(E_{\rm cm}) = \frac{m_\pi}{E_{\rm cm}}\frac{a_i + b_i\Delta_{\pi\Sigma}(E_{\rm cm})}{1 + c_i\Delta_{\pi\Sigma}(E_{\rm cm})}. \tag{19}$$

Making use of these forms for $\widetilde{K}$, fits are carried out to determine the best-fit values of the above parameters using the spectrum method [85]. The correlated-χ^2 minimized in these fits is defined similar to Eq. (14) in Ref. [46], except that the residuals are formed in terms of differences between the center-of-mass energy interaction shifts $\Delta E_{\rm cm}$ obtained from the quantization condition using the $\widetilde{K}$-matrix parametrization and the interaction shifts determined from the Monte Carlo computations. For each of the four parametrizations above, several fits were carried out, setting various parameters to zero to check sensitivity to these parameters. The results are presented in Tables VIII to XI of Appendix C. In these tables, statistical uncertainties are estimated using a simple derivative method, as described in Ref. [46]. This method is faster than other methods, but it often yields slightly underestimated values. However, this method is sufficient for the purposes of illustrating model dependence. Each fit in these tables also shows the value of the Akaike Information Criterion (AIC) [86] defined by

$$\text{AIC} = \chi^2 - 2\,n_{\rm dof}, \tag{20}$$

where $n_{\rm dof}$ denotes the number of degrees of freedom.

The best-fit values for the $\widetilde{K}$-matrix parameters in Tables VIII to XI show large variations from fit to fit. However, only more physically-relevant quantities, such as the scattering amplitudes or the S-matrix pole positions, are important. We define a quantity $t_{ij}^{(J^P)}(E_{\rm cm})$ which is proportional to the scattering transition amplitude and is related to $\widetilde{K}$ by

$$t^{-1} = \widetilde{K}^{-1} - i\widehat{k}, \tag{21}$$

where $\widehat{k} = \text{diag}\,(k_{\pi\Sigma}, k_{\bar{K}N})$. The different parametrizations discussed above constrain the energy dependence of the amplitudes near the finite-volume energies, even if they do not accommodate left-hand (cross-channel) cuts. Knowledge over this limited range enables the analytic continuation of $t_{ij}(E_{\rm cm})$ to complex $E_{\rm cm}$ and the identification of poles close to the real axis on sheets adjacent to the physical one. Analytic continuation of the coupled channel $\pi\Sigma - \bar{K}N$ scattering amplitude involves four different Riemann sheets, each labelled by the sign of the imaginary parts of $(k_{\pi\Sigma}, k_{\bar{K}N})$, with $(+,+)$ denoting the physical sheet. Complex poles in the scattering amplitudes correspond to vanishing eigenvalues in the right-hand side of Eq. (21) and are determined numerically. In the vicinity of a pole, the divergent part of the amplitude is

$$t = \frac{1}{E_{\rm cm} - E_{\rm pole}}\begin{pmatrix} c_{\pi\Sigma}^2 & c_{\pi\Sigma}\,c_{\bar{K}N} \\ c_{\pi\Sigma}\,c_{\bar{K}N} & c_{\bar{K}N}^2 \end{pmatrix} + \ldots, \tag{22}$$

where the (complex) residues $c_{\pi\Sigma}$, $c_{\bar{K}N}$ represent the coupling of the resonance pole to each channel.

Results for the scattering transition amplitudes and the pole locations for each of the fits in Tables VIII to XI are shown in Fig. 6. The transition amplitudes are shown in the upper panel, and the resulting poles from the analytic continuations are shown in the middle panel of Fig. 6. Each line in the upper panel corresponds to a different fit in Tables VIII to XI, with corresponding pairs of points in the middle panel. The transparency of the lines and points is directly related to the value of the AIC, darker implying a lower AIC. One sees that the variations between the results of the transition amplitudes and the S-matrix poles from the different fits are no longer large.

The first parametrization, given by Eq. (13), leads to the lowest AIC, i.e. $\text{AIC}_{\rm min}$. Given this, a fit is carried out using this parametrization and the errors are more accurately determined using a bootstrap procedure with 800 samples. The fit with the lowest AIC value is a four-parameter fit of the form of Eq. (13), and the best-fit

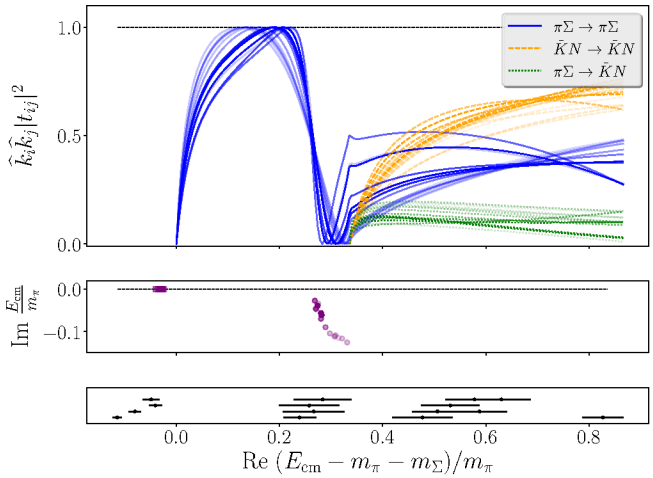

FIG. 6. Scattering amplitudes and S-matrix pole locations against center-of-mass energy difference to the $\pi\Sigma$ threshold for various fits using the four different $\widetilde{K}$-matrix parametrizations. The quantities t and $\hat{k}$ are defined in Eq. (21), and the subscripts i, j refer to the flavor channels. The different fits in Tables VIII to XI are shown as different lines in the upper panel, with corresponding pairs of points in the middle panel which show the positions of the S-matrix poles in the complex center-of-mass energy plane. The transparency parameter in matplotlib [87] of each line and corresponding pair of points is set to be $\texttt{alpha} = \exp(-(\mathrm{AIC} - \mathrm{AIC}_{\rm min})/2)$. The bottom panel shows the finite-volume spectrum used to constrain the fits involving the transition amplitudes.

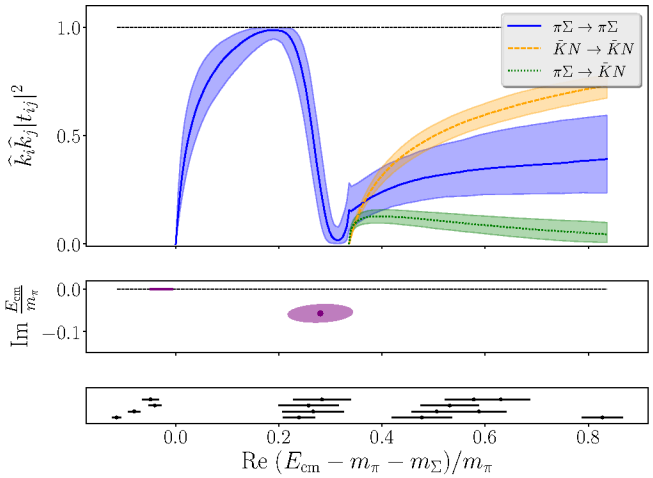

FIG. 7. The isospin $I = 0$ and strangeness $S = -1$ coupled-channel $\pi\Sigma - \bar{K}N$ transition amplitudes computed on a single lattice QCD gauge-field ensemble with $m_\pi \approx 200\,\mathrm{MeV}$ as a function of the center-of-mass energy difference to the $\pi\Sigma$ threshold. Results are obtained using the best fit specified by Eqs. (23) and (13), with uncertainties estimated by bootstrap resampling. The quantities t and $\hat{k}$ are defined in Eq. (21), and the subscripts i, j refer to the flavor channels. The middle panel shows the positions of the S-matrix poles in the complex center-of-mass energy plane on the sheets closest to the physical one. The bottom panel shows the finite-volume spectrum used to constrain the fits involving the transition amplitudes.

parameters values are

$$\begin{aligned} A_{00} &= 4.1(1.8), \qquad A_{11} = -10.5(1.1), \\ A_{01} &= 10.3(1.5), \qquad B_{01} = -29(18), \end{aligned} \tag{23}$$

with fixed $B_{00} = B_{11} = 0$ and $\chi^2 = 10.52$ for 11 degrees of freedom. This fit is shown in Fig. 7. The finite-volume energies that are used in this fit are shown in Fig. 8. The green points show the center-of-mass energies obtained from the Monte Carlo lattice QCD computations, and the blue points show the energies obtained from the fit using the quantization condition and the $\widetilde{K}$-matrix parametrization of Eq. (13) with best-fit values given in Eq. (23).

For this preferred fit, two poles are found on the $(-,+)$ sheet, which is the one closest to physical scattering in the region between the two thresholds, with energies

$$\begin{aligned} E_1/m_\pi &= 6.856(45)_{\rm st}(06)_{\rm md}, \\ E_2/m_\pi &= 7.144(63)_{\rm st}(07)_{\rm md} - i\,0.057(22)_{\rm st}(17)_{\rm md}, \end{aligned}$$

$$\begin{aligned} E_1 &= 1392(9)_{\rm st}(2)_{\rm md}(16)_a \text{ MeV} \\ E_2 &= [1455(13)_{\rm st}(2)_{\rm md}(17)_a \\ &\quad - i \times 11.5(4.4)_{\rm st}(4)_{\rm md}(0.1)_a] \text{ MeV}, \end{aligned} \tag{24}$$

while their couplings are

$$\begin{aligned} c^{(1)}_{\pi\Sigma} &= i\,0.52(10)_{\rm st}(2)_{\rm md}, \\ c^{(1)}_{\bar{K}N} &= i\,0.28(8)_{\rm st}(6)_{\rm md}, \\ c^{(2)}_{\pi\Sigma} &= 0.26(9)_{\rm st}(5)_{\rm md} - i\,0.13(3)_{\rm st}(3)_{\rm md}, \\ c^{(2)}_{\bar{K}N} &= 0.12(6)_{\rm st}(4)_{\rm md} - i\,0.53(4)_{\rm st}(2)_{\rm md}. \end{aligned} \tag{25}$$

The ratios of these couplings (with correlated uncertainties) show that the lower pole is more strongly coupled to the $\pi\Sigma$ channel, while the pole at a larger real energy is more strongly coupled to the $\bar{K}N$ channel:

$$\begin{aligned} \left| \frac{c^{(1)}_{\pi\Sigma}}{c^{(1)}_{\bar{K}N}} \right| &= 1.9(4)_{\rm st}(6)_{\rm md}, \\ \left| \frac{c^{(2)}_{\pi\Sigma}}{c^{(2)}_{\bar{K}N}} \right| &= 0.53(9)_{\rm st}(10)_{\rm md}. \end{aligned} \tag{26}$$

In the above results, the first uncertainty is statistical, the second accounts for the model parametrization dependence, and when the pole positions are quoted in physical units, the third comes from the scale setting uncertainty in Table I. For this work, the systematic uncertainty due to the parametrization dependence is estimated by considering all models with $\mathrm{AIC} - \mathrm{AIC}_{\rm min} < 1$, and taking half the difference in the maximal spread of

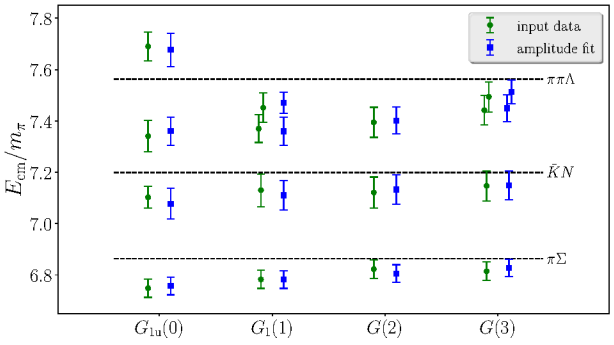

FIG. 8. Finite-volume spectrum in the center-of-mass frame used as input data to constrain parametrizations of the coupled-channel $\pi\Sigma$-$\bar{K}N$ scattering amplitude (green circles). Each column corresponds to a particular irrep $\Lambda(\boldsymbol{d}^2)$ of the little group of total momentum $\boldsymbol{P}^2 = (2\pi/L)^2\boldsymbol{d}^2$. Only irreps where the $\ell = 0$ partial wave contributes are included. Dashed lines indicate various thresholds, as labeled. Model energies from the resultant fit are shown as blue squares.

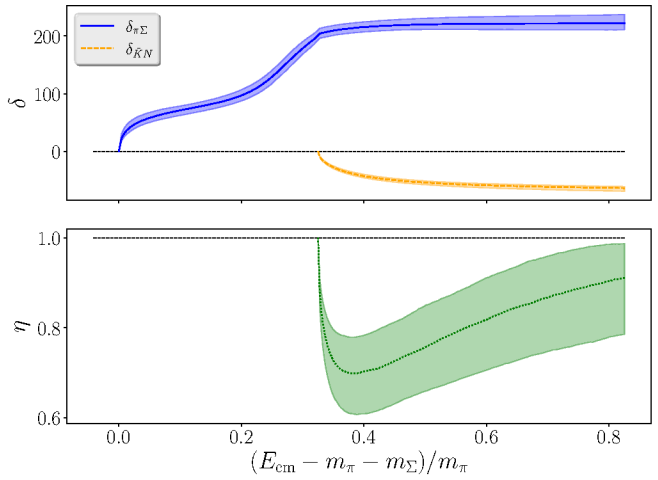

FIG. 9. Inelasticity η and phase shifts $\delta_{\pi\Sigma}$ and $\delta_{\bar{K}N}$ against center-of-mass energy difference to the $\pi\Sigma$ threshold. These quantities are defined in Eq. (27). Results are obtained using the best fit specified by Eqs. (23) and (13), with uncertainties estimated by bootstrap resampling.

values as the model uncertainty. In future work, when a full extrapolation to the physical point is performed, a more thorough determination of the model-average and systematic uncertainty will be performed.

As shown in Fig. 6, the existence of two poles remains robust under variations of the underlying parametrization of the K-matrix. Our $\widetilde{K}$-matrix parametrizations make no assumptions about the number or locations of the S-matrix poles, and can accommodate zero, one, or two poles. The pole at E_1 is most likely a virtual bound state (except in 0.5% of the bootstrap samples where the pole is in the physical sheet and is thus a bound state), while the one at E_2 is a resonance. The first pole has a stronger coupling to $\pi\Sigma$, while the second couples more strongly to $\bar{K}N$.

Another way of presenting the results for the amplitudes is to show the scattering phase shifts δ_i and the inelasticity η, which are related to t by

$$\begin{aligned} t_{00} &= \frac{\eta e^{2i\delta_{\pi\Sigma}} - 1}{2ik_{\pi\Sigma}}, \\ t_{11} &= \frac{\eta e^{2i\delta_{\bar{K}N}} - 1}{2ik_{\bar{K}N}}, \\ t_{01} &= \frac{\sqrt{1-\eta^2}\, e^{i(\delta_{\pi\Sigma}+\delta_{\bar{K}N})}}{2\sqrt{k_{\pi\Sigma}k_{\bar{K}N}}}, \end{aligned} \tag{27}$$

where the indices again indicate the flavor channel: 0 for $\pi\Sigma$ and 1 for $\bar{K}N$. The results are shown in Fig. 9. This figure illustrates two features that can be related to the two-pole structure. First, a rapid increase of the phase at the $\Sigma\pi$ threshold is related to the presence of a close virtual bound state. Second, the phase crosses 90 degrees near the position of the real part of the second pole.

C. Single-channel $\pi\Sigma$ scattering

In the vicinity of the $\pi\Sigma$ threshold, and well below the $\bar{K}N$ threshold, the standard single-channel Lüscher formalism can be used to study the elastic $\pi\Sigma$ scattering amplitude. Compared to the multi-channel approach, the single-channel approach is equivalent up to effects that are exponentially-suppressed with respect to the distance to the $\bar{K}N$ threshold. Such an analysis is used here to show further evidence of the existence of the lower pole and its nature as a virtual bound state.

We perform this single-channel analysis using the lowest energies in each frame in the $G_{1u}(0), G_1(1)$, $G(2)$ and $G(3)$ irreps (4 in total), as shown in Fig. 8. The elastic scattering phase shift can be parametrized by

$$\frac{k_{\pi\Sigma}}{m_\pi}\cot\delta_{\pi\Sigma} = E_{\rm cm}(a_{\pi\Sigma} + b_{\pi\Sigma}\Delta_{\pi\Sigma}), \tag{28}$$

where $a_{\pi\Sigma}$ and $b_{\pi\Sigma}$ are fit parameters. The results of performing a fit using the spectrum method as in Ref. [46] are

$$a_{\pi\Sigma} = 0.047(14), \quad b_{\pi\Sigma} = 0.65(50), \quad \chi^2 = 5.04, \tag{29}$$

with 2 degrees of freedom. A visualization of the single-channel phase shift from the fit is shown in Fig. 10, along with a comparison to the elastic phase shift from the multi-channel analysis in Eq. (23). One observes that the phase shift curve (blue band) intersects the virtual bound state condition (black dashed line). That is,

$$k_{\pi\Sigma}\cot\delta_{\pi\Sigma} - ik_{\pi\Sigma} = 0, \tag{30}$$

for purely imaginary and negative $k_{\pi\Sigma}$. The position of

the virtual bound state is found at

$$E_1/m_\pi = 6.822(37), \quad E_1 = 1389(8)_{\rm st}(16)_a \text{ MeV}. \tag{31}$$

Thus, the results are consistent with those obtained in the multichannel analysis, and confirm the existence of the lower pole in a model-independent way. The larger χ^2 per degree of freedom compared to the multi-channel analysis may arise from the proximity of the $\bar{K}N$ threshold, suggesting the need for the multi-channel approach to study this system.

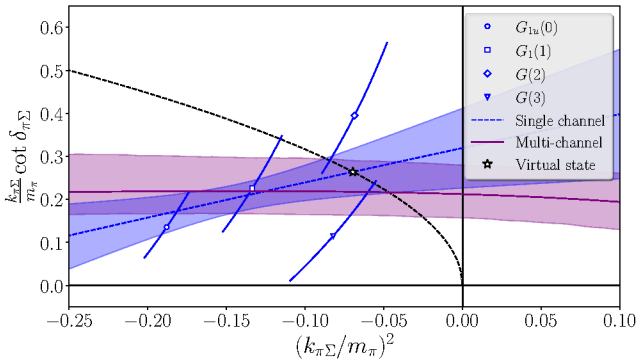

FIG. 10. The $\pi\Sigma$ elastic phase shift as a function of the center-of-mass momentum squared, determined in a single-channel analysis and compared against the multi-channel result. The dashed black line corresponds to the virtual bound state condition in Eq. (30). The blue dashed line and corresponding band show the fit to an effective range expansion with statistical errors. The star labels the position of the virtual bound state in the single-channel analysis. The solid purple line and the associated band show the result from the multi-channel fit with lowest AIC value. The scattering phase shifts from each energy level are shown by the hollow blue symbols.

D. Effect of higher partial waves

The analysis above only includes s waves and the $J^P = 1/2^-$ amplitudes. For the energies in the rest frame in the $G_{1u}(0)$ irrep, this is a good approximation, since this irrep only receives contamination from $\ell = 4$ partial waves. By contrast, energy levels in moving frames, such as the $G_1(1)$, $G(2)$, and $G(3)$ irreps, receive contamination from p-waves. In particular, the dominant contamination from higher partial waves is expected to be from the $J^P = 1/2^+$ and $J^P = 3/2^+$ channels. The scattering amplitude for $J^P = 1/2^+$ is the leading contribution to the finite-volume energy shifts in the $G_{1g}(0)$ irrep, while in the $F_1(3)$ and $F_2(3)$ irreps, the $J^P = 3/2^+$ wave dominates. Since a few energy levels in these irreps are determined in this work, as shown in Fig. 5, we can use these energies to estimate the strength of the interactions in these two waves and how they impact the main fit of this work.

To assess this, we perform two additional fits. In the first additional fit, sixteen energies are used, which include the fifteen energies from the s-wave fits and one $G_{1g}(0)$ level, and we incorporate a $J^P = 1/2^+$ wave in the $\widetilde{K}$-matrix parametrization. In the second additional fit, seventeen energies are used, which include the fifteen energies from the s-wave fits and one level each in the $F_1(3), F_2(3)$ irreps, and we add a $J^P = 3/2^+$ wave in the $\widetilde{K}$-matrix parametrization. For each of these additional partial waves, we use simple parametrizations of the form

$$\tilde{K}^{J^P} = \text{diag}\left(A_{00}^{J^P}, A_{11}^{J^P}\right). \tag{32}$$

The results of these additional fits are presented in Table XII of Appendix C. One sees that the shifts in the parameters due to considering additional waves is about an order of magnitude lower than the statistical uncertainty when considering only the leading partial wave. Thus, it can be concluded that the effects of higher partial waves can be neglected to the present statistical uncertainty for energies below the $\pi\pi\Lambda$ threshold.

IV. CONCLUSION

Hermitian correlation matrices using both single baryon and meson-baryon interpolating operators for a variety of different total momenta and irreducible representations were used to determine the finite-volume stationary-state energies in the isospin $I = 0$ strangeness $S = -1$ sector in lattice QCD with the stochastic LapH method. Results were obtained using a single ensemble of gauge field configurations with $N_f = 2 + 1$ dynamical quark flavors and $m_\pi \approx 200$ MeV and $m_K \approx 487$ MeV on a $64^3 \times 128$ lattice with spacing $a = 0.0633(4)(6)$ fm. Various K-matrix parametrizations restricted to s-waves were then employed in the quantization condition to match the spectrum obtained from lattice QCD. The resulting best-fit parameter values from the K-matrix parametrization yielding the lowest Akaike Information Criterion produced the $\pi\Sigma$-$\bar{K}N$ transition amplitudes shown in Fig. 7. Analytic continuation of the transition amplitudes into complex center-of-mass energies revealed two poles, suggesting a virtual bound state below the $\pi\Sigma$ threshold and a resonance just below the higher $\bar{K}N$ threshold. A single channel fit of $\pi\Sigma$ scattering showed the robustness of the lower pole, and the effects of including the leading p-wave contributions were examined and found to be negligible at the current statistical precision.

The results presented here demonstrate the feasibility of using current lattice QCD techniques to study coupled-channel dynamics for baryon resonances such as the controversial $\Lambda(1405)$. We plan to obtain results at physical quark masses, as well as results for several lattice spacings to extrapolate to the continuum-limit. The importance of studying lattice spacing errors has been underscored recently by the observation of large discretization effects in the H-dibaryon binding energy[88] using the

same lattice discretization as employed here. However, that work suggests that at the fine lattice spacing used here the result is unlikely to differ qualitatively from the continuum. Note that moving to physical quark masses requires the consideration of three-particle effects due to $\pi\pi\Lambda$ states. The lattice QCD determination of levels above this threshold should not present a major problem in the region relevant for the $\Lambda(1405)$, and the formalism for three-hadrons including particles with spin is progressing rapidly [89]. Exploring the quark-mass trajectory toward the SU(3)-symmetric point will be useful for testing chiral effective theories. This work opens the door to investigating other baryon resonances, such as the $N(1535)$, $\Lambda(1670)$, $\Sigma(1620)$, and $\Xi(1620)$, among others.

ACKNOWLEDGMENTS

We acknowledge helpful discussions with R.J. Hudspith, A. Jackura, M.F.M. Lutz and M. Mai. We thank our colleagues within the CLS consortium for sharing ensembles. Computations were carried out on Frontera [90] at the Texas Advanced Computing Center (TACC), and at the National Energy Research Scientific Computing Center (NERSC), a U.S. Department of Energy Office of Science User Facility located at Lawrence Berkeley National Laboratory, operated under Contract No. DE-AC02-05CH11231 using NERSC awards NP-ERCAP0005287, NP-ERCAP0010836 and NP-ERCAP0015497. This work was supported in part by: the U.S. National Science Foundation under awards PHY-1913158 and PHY-2209167 (CJM and SK), the Faculty Early Career Development Program (CAREER) under award PHY-2047185 (AN) and by the Graduate Research Fellowship Program under Grant No. DGE-2040435 (JM); the U.S. Department of Energy, Office of Science, Office of Nuclear Physics, under grant contract numbers DE-SC0011090 and DE-SC0021006 (FRL), DE-SC0012704 (ADH), DE-AC02-05CH11231 (AWL) and within the framework of Scientific Discovery through Advanced Computing (SciDAC) award "Fundamental Nuclear Physics at the Exascale and Beyond" (ADH); the Mauricio and Carlota Botton Fellowship (FRL); and the Heisenberg Programme of the Deutsche Forschungsgemeinschaft (DFG, German Research Foundation) project number 454605793 (DM). NumPy [91], matplotlib [87], and the CHROMA software suite [92] were used for analysis, plotting, and correlator evaluation.

Appendix A: Single- and two-hadron operators

The single- and two-hadron operators used in this study are specified in Tables IV-VII in this section. We use multi-hadron operators comprised of individual constituent hadrons, each corresponding to a definite momentum. Each single-hadron operator is specified by its flavor structure, such as Λ, Σ, N, π, $\bar{K}$, then in square brackets, the irrep of its little group, with the squared spatial momentum, in units of $(2\pi/L)^2$, shown in parentheses. The subscript indicates a spatial identification number. The spin and orbital structure associated with each identification number can be obtained from the authors upon request.

All operators used in this study are single-site operators. The notation for the irreps follows the conventions in Ref. [63]. The subscripts g/u denote even/odd parity, and the superscripts $+/-$ denote even/odd G-parity. Whenever there are more than one independent Clebsch-Gordan combinations, the multiplicity is indicated by an integer in parentheses to the right of the operator identification. The Clebsch-Gordan coefficients that fully define each operator are not given, but are available upon request.

TABLE IV. Single- and two-hadron operators used in each symmetry sector with total momentum $\boldsymbol{d}^2 = 0$. Operator notation is described in the text.

$\Lambda(\boldsymbol{d}^2)$	Operators
$H_\mathrm{u}(0)$	$\pi[A_{1u}^-(0)]_0\ \Sigma[Hg(0)]_0$
	$\pi[A_2^-(1)]_1\ \Sigma[G_1(1)]_0$
	$\bar{K}[A_2(1)]_1\ N[G_1(1)]_0$
$G_{1\mathrm{g}}(0)$	$\Lambda[G_{1g}(0)]_0$
	$\Lambda[G_{1g}(0)]_1$
	$\Lambda[G_{1g}(0)]_3$
	$\bar{K}[A_2(1)]_1\ N[G_1(1)]_0$
	$\pi[A_2^-(1)]_1\ \Sigma[G_1(1)]_0$
$G_{1\mathrm{u}}(0)$	$\Lambda[G_{1u}(0)]_0$
	$\Lambda[G_{1u}(0)]_1$
	$\Lambda[G_{1u}(0)]_2$
	$\Lambda[G_{1u}(0)]_3$
	$\bar{K}[A_{1u}(0)]_0\ N[G_{1g}(0)]_0$
	$\pi[A_{1u}^-(0)]_0\ \Sigma[G_{1g}(0)]_0$
	$\bar{K}[A_2(1)]_1\ N[G_1(1)]_0$
	$\pi[A_2^-(1)]_1\ \Sigma[G_1(1)]_0$

TABLE V. Same as Table IV with $\boldsymbol{d}^2 = 1$.

$\Lambda(\boldsymbol{d}^2)$	Operators
$G_1(1)$	$\Lambda[G_1(1)]_0$
	$\Lambda[G_1(1)]_1$
	$\Lambda[G_1(1)]_2$
	$\Lambda[G_1(1)]_4$
	$\Lambda[G_1(1)]_6$
	$\bar{K}[A_{1u}(0)]_0\ N[G_1(1)]_0$
	$\pi[A_{1u}^-(0)]_0\ \Sigma[G_1(1)]_0$
	$\bar{K}[A_2(1)]_1\ N[G_1g(0)]_0$
	$\pi[A_2^-(1)]_1\ \Sigma[G_1g(0)]_0$
$G_2(1)$	$\Lambda[G_2(1)]_0$
	$\Lambda[G_2(1)]_1$
	$\pi[A_{1u}^-(0)]_0\ \Sigma[G_2(1)]_0$
	$\pi[A_2^-(1)]_1\ \Sigma[G(2)]_0 \quad (2)$
	$\bar{K}[A_2(1)]_1\ N[G(2)]_0 \quad (2)$

TABLE VI. Same as Table IV with $\boldsymbol{d}^2 = 2$.

$\Lambda(\boldsymbol{d}^2)$	Operators
$G(2)$	$\Lambda[G(2)]_0$
	$\Lambda[G(2)]_1$
	$\Lambda[G(2)]_2$
	$\Lambda[G(2)]_3$
	$\Lambda[G(2)]_5$
	$\Lambda[G(2)]_6$
	$\bar{K}[A_{1u}(0)]_0\ N[G(2)]_0$
	$\pi[A_{1u}^-(0)]_0\ \Sigma[G(2)]_0$
	$\bar{K}[A_2(1)]_1\ N[G_1(1)]_0$ (2)
	$\pi[A_2^-(1)]_1\ \Sigma[G_1(1)]_0$ (2)
	$\bar{K}[A_2(2)]_0\ N[G_{1g}(0)]_0$
	$\pi[A_{1u}^-(0)]_0\ \Sigma[G(2)]_1$
	$\pi[A_{1u}^-(0)]_0\ \Sigma[G(2)]_7$

TABLE VII. Same as Table IV with $\boldsymbol{d}^2 = 3$.

$\Lambda(\boldsymbol{d}^2)$	Operators
$F_1(3)$	$\Lambda[F_1(3)]_0$
	$\pi[A_2^-(1)]_1\ \Sigma[G(2)]_0$
	$\bar{K}[A_2(1)]_1\ N[G(2)]_0$
	$\pi[A_2^-(2)]_0\ \Sigma[G_1(1)]_0$
	$\bar{K}[A_2(2)]_0\ N[G_1(1)]_0$
	$\pi[A_{1u}^-(0)]_0\ \Sigma[F_2(3)]_0$
$F_2(3)$	$\Lambda[F_2(3)]_0$
	$\pi[A_2^-(1)]_1\ \Sigma[G(2)]_0$
	$\bar{K}[A_2(1)]_1\ N[G(2)]_0$
	$\pi[A_2^-(2)]_0\ \Sigma[G_1(1)]_0$
	$\bar{K}[A_2(2)]_0\ N[G_1(1)]_0$
	$\pi[A_{1u}^-(0)]_0\ \Sigma[F_1(3)]_0$
$G(3)$	$\Lambda[G(3)]_0$
	$\Lambda[G(3)]_1$
	$\Lambda[G(3)]_4$
	$\Lambda[G(3)]_5$
	$\bar{K}[A_{1u}(0)]_0\ N[G(3)]_0$
	$\pi[A_{1u}^-(0)]_0\ \Sigma[G(3)]_0$
	$\bar{K}[A_2(1)]_1\ N[G(2)]_0$ (2)
	$\pi[A_2^-(1)]_1\ \Sigma[G(2)]_0$ (2)
	$\bar{K}[A_2(2)]_0\ N[G_1(1)]_0$ (2)
	$\bar{K}[A_2(2)]_0\ N[G_{1g}(0)]_0$

Appendix B: Energy extractions

Energy determinations are shown in Fig. 11 in this section. Results from four different fit methods are shown: two-exponential and geometric-exp series fits to the rotated correlator, and single-exponential fits to the ratio of the rotated diagonal correlator over the product of single-hadron correlators for either $\bar{K}(\boldsymbol{d}_{\bar{K}}^2)N(\boldsymbol{d}_N^2)$ or $\pi(\boldsymbol{d}_\pi^2)\Sigma(\boldsymbol{d}_\Sigma^2)$. The dark horizontal band and filled symbol denote the final chosen fit for each level selected as described in the Sec. II C.

Appendix C: Amplitude parameter fit results

Best-fit results for the parameters in the various $\widetilde{K}$-matrix parametrizations are presented here. Results are obtained by fitting the spectrum obtained from the $\widetilde{K}$-matrix parametrizations and the quantization condition to the spectrum determined in the lattice QCD computations. Tables VIII-XI contain results from fits using $\ell_{\max} = 0$, and Table XII using $\ell_{\max} = 1$.

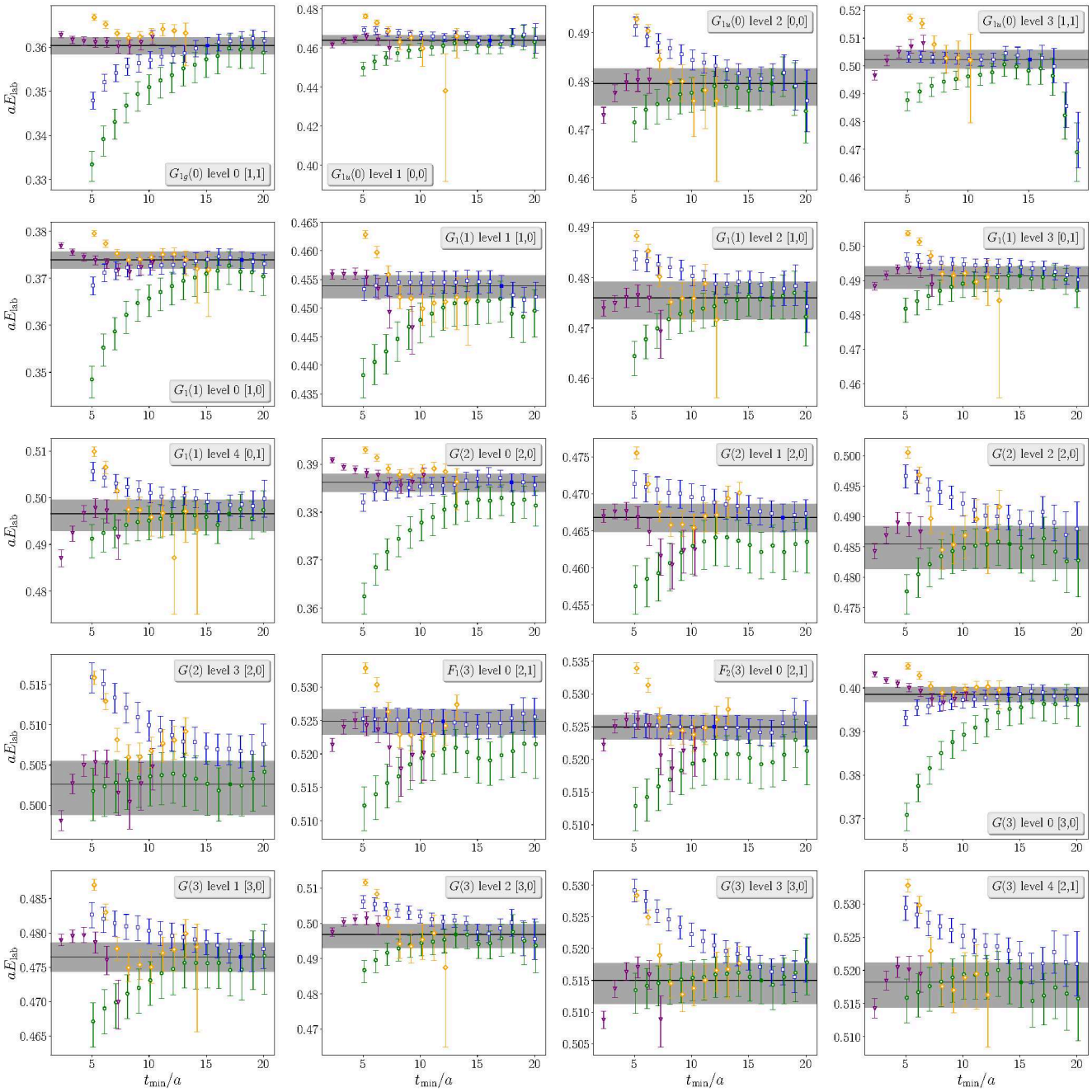

FIG. 11. Fit results for the stationary-state energies indicated. These plots are similar to that shown in Fig. 4. Orange diamonds and purple triangles indicate results from fits using a two-exponential and a geometric-exp series, respectively. Green circles and blue squares indicate results from single-exponential fits to ratios of the rotated diagonal correlator over the product of $N(\boldsymbol{d}_1^2)\ \overline{K}(\boldsymbol{d}_2^2)$ and $\Sigma(\boldsymbol{d}_1^2)\ \pi(\boldsymbol{d}_2^2)$ single-hadron correlators, respectively, as described in Sec. II C. In each plot, the integers in square brackets in the legend show the values $[\boldsymbol{d}_1^2, \boldsymbol{d}_2^2]$. The dark horizontal band and filled symbol denote the final chosen fit selected as described in Sec. II C.

TABLE VIII. Fit results for $\widetilde{K}$ parametrization class 1 shown in Eq. (13). Errors are propagated through the derivative method. Empty entries indicate parameters set to zero in a fit. AIC refers to Akaike Information Criterion.

Fit	A_{00}	A_{11}	A_{01}	B_{00}	B_{11}	B_{01}	χ^2/dof	AIC
a	1.5(1.4)	−8.78(72)	8.30(65)				15.68/(15 − 3)	−8.32
b	4.1(1.2)	−10.5(1.1)	10.3(1.3)			−29(15)	10.52/(15 − 4)	−11.48
c	2.3(1.3)	−8.62(58)	7.60(80)		−18(11)		12.29/(15 − 4)	−9.71
d	15.1(5.3)	−11.8(1.3)	7.6(1.3)	−56(19)			11.48/(15 − 4)	−10.52
e	9.6(6.2)	−12.7(3.4)	11.1(2.8)	−23(26)	18(31)	−37(29)	9.70/(15 − 6)	−8.30

TABLE IX. Fit results for $\widetilde{K}$ parametrization class 2 shown in Eq. (14). Errors are propagated through the derivative method. Empty entries indicate parameters set to zero in a fit. AIC refers to Akaike Information Criterion.

Fit	$\widehat{A}_{00}$	$\widehat{A}_{11}$	$\widehat{A}_{01}$	$\widehat{B}_{00}$	$\widehat{B}_{11}$	$\widehat{B}_{01}$	χ^2/dof	AIC
a	0.16(19)	−1.229(91)	1.140(88)				15.44/(15 − 3)	−8.56
b	0.52(18)	−1.45(15)	1.42(18)			−3.9(2.0)	10.73/(15 − 4)	−11.27

TABLE X. Fit results for $\widetilde{K}$ parametrization class 3 shown in Eq. (15). Errors are propagated through the derivative method. Empty entries indicate parameters set to zero in a fit. AIC refers to Akaike Information Criterion.

Fit	$\widetilde{A}_{00}$	$\widetilde{A}_{11}$	$\widetilde{A}_{01}$	$\widetilde{B}_{00}$	$\widetilde{B}_{11}$	$\widetilde{B}_{01}$	χ^2/dof	AIC
a	0.092(21)	−0.036(15)	0.082(20)	0.28(15)			11.73/(15 − 4)	−10.27
b	0.114(25)	−0.041(24)	0.096(19)		0.19(16)		14.57/(15 − 4)	−7.43
c	0.137(33)	−0.019(14)	0.119(21)			−0.142(85)	13.10/(15 − 4)	−8.90

TABLE XI. Fit results for $\widetilde{K}$ parametrization class 4 shown in Eq. (16). Errors are propagated through the derivative method. Empty entries indicate parameters set to zero in a fit. AIC refers to Akaike Information Criterion.

Fit	a_0	a_1	b_0	b_1	c_0	c_1	ϵ	χ^2/dof	AIC
a	5.7(1.2)	−11.4(1.2)		−27(15)			0.451(56)	13.27/(15 − 4)	−8.73
b	13.7(4.1)	−14.06(86)	−37(17)				0.349(75)	10.63/(15 − 4)	−11.37
c	5.8(1.2)	−11.8(1.1)				−1.62(95)	0.468(48)	13.54/(15 − 4)	−8.46
d	12.2(3.4)	−14.06(87)			5.8(3.2)		0.360(82)	11.13/(15 − 4)	−10.87

TABLE XII. Fit results for $\widetilde{K}$ parametrization class 1 shown in Eq. (13) for the $J^P = 1/2^-$ wave, and Eq. (32) for the $J^P = 1/2^+, 3/2^+$ waves using $\ell_{\max} = 1$. Errors are propagated through the derivative method. Empty entries indicate parameters set to zero in a fit. AIC refers to Akaike Information Criterion.

J^P partial waves	A_{00}	A_{11}	A_{01}	B_{01}	$A_{00}^{1/2^+}$	$A_{11}^{1/2^+}$	$A_{00}^{3/2^+}$	$A_{11}^{3/2^+}$	χ^2/dof	AIC
$1/2^-$	4.1(1.2)	−10.5(1.1)	10.3(1.3)	−29(15)					10.52/(15-4)	−11.48
$1/2^-$ and $1/2^+$	4.1(1.2)	−10.5(1.1)	10.3(1.3)	−30(15)	0.0088(39)	0.031(15)			10.52/(17-6)	−11.48
$1/2^-$ and $3/2^+$	4.1(1.1)	−10.9(1.1)	10.4(1.3)	−32(15)			0.0172(48)	0.0218(48)	14.10/(21-6)	−15.90

[1] R. L. Workman *et al.* (Particle Data Group), Review of Particle Physics, PTEP **2022**, 083C01 (2022).

[2] R. H. Dalitz and S. F. Tuan, Possible resonant state in pion-hyperon scattering, Phys. Rev. Lett. **2**, 425 (1959).

[3] R. H. Dalitz and S. F. Tuan, The phenomenological representation of $\overline{K}$-nucleon scattering and reaction amplitudes, Annals Phys. **10**, 307 (1960).

[4] T. Hyodo and D. Jido, The nature of the $\Lambda(1405)$ resonance in chiral dynamics, Prog. Part. Nucl. Phys. **67**, 55 (2012), arXiv:1104.4474 [nucl-th].

[5] T. Hyodo and M. Niiyama, QCD and the strange baryon spectrum, Prog. Part. Nucl. Phys. **120**, 103868 (2021), arXiv:2010.07592 [hep-ph].

[6] M. Bazzi *et al.* (SIDDHARTA), A New Measurement of Kaonic Hydrogen X-rays, Phys. Lett. B **704**, 113 (2011), arXiv:1105.3090 [nucl-ex].

[7] U. G. Meissner, U. Raha, and A. Rusetsky, Spectrum and decays of kaonic hydrogen, Eur. Phys. J. C **35**, 349 (2004), arXiv:hep-ph/0402261.

[8] K. Moriya *et al.* (CLAS), Measurement of the $\Sigma\pi$ photoproduction line shapes near the $\Lambda(1405)$, Phys. Rev. C **87**, 035206 (2013), arXiv:1301.5000 [nucl-ex].

[9] K. Moriya *et al.* (CLAS), Spin and parity measurement of the Lambda(1405) baryon, Phys. Rev. Lett. **112**, 082004 (2014), arXiv:1402.2296 [hep-ex].

[10] M. Mai and U.-G. Meißner, Constraints on the chiral unitary $\bar{K}N$ amplitude from $\pi\Sigma K^+$ photoproduction data, Eur. Phys. J. A **51**, 30 (2015), arXiv:1411.7884 [hep-ph].

[11] L. Roca and E. Oset, Isospin 0 and 1 resonances from $\pi\Sigma$ photoproduction data, Phys. Rev. C **88**, 055206 (2013), arXiv:1307.5752 [nucl-th].

[12] G. Scheluchin *et al.* (BGOOD), Photoproduction of $K^+\Lambda(1405) \to K^+\pi^0\Sigma^0$ extending to forward angles and low momentum transfer, Phys. Lett. B **833**, 137375 (2022), arXiv:2108.12235 [nucl-ex].

[13] S. Acharya *et al.* (ALICE), Constraining the $\overline{K}N$ coupled channel dynamics using femtoscopic correlations at the LHC, Eur. Phys. J. C **83**, 340 (2023), arXiv:2205.15176 [nucl-ex].

[14] N. Wickramaarachchi, R. A. Schumacher, and G. Kalicy (GlueX), Decay of the $\Lambda(1405)$ hyperon to Σ^0 π^0 measured at GlueX, EPJ Web Conf. **271**, 07005 (2022), arXiv:2209.06230 [nucl-ex].

[15] S. Aikawa *et al.* (J-PARC E31), Pole position of $\Lambda(1405)$ measured in d(K^-,n)π Σ reactions, Phys. Lett. B **837**, 137637 (2023), arXiv:2209.08254 [nucl-ex].

[16] A. V. Anisovich, A. V. Sarantsev, V. A. Nikonov, V. Burkert, R. A. Schumacher, U. Thoma, and E. Klempt, Hyperon III: $K^-p - \pi\Sigma$ coupled-channel dynamics in the $\Lambda(1405)$ mass region, Eur. Phys. J. A **56**, 139 (2020).

[17] N. Isgur and G. Karl, P Wave Baryons in the Quark Model, Phys. Rev. D **18**, 4187 (1978).

[18] J. A. Oller and U. G. Meissner, Chiral dynamics in the presence of bound states: Kaon nucleon interactions revisited, Phys. Lett. B **500**, 263 (2001), arXiv:hep-ph/0011146.

[19] M. Mai, Status of the $\Lambda(1405)$, Few Body Syst. **59**, 61 (2018).

[20] M. Mai, Review of the $\Lambda(1405)$ A curious case of a strangeness resonance, Eur. Phys. J. ST **230**, 1593 (2021), arXiv:2010.00056 [nucl-th].

[21] T. Ezoe and A. Hosaka, $\Lambda(1405)$ as a $\overline{K}N$ Feshbach resonance in the Skyrme model, Phys. Rev. D **102**, 014046 (2020), arXiv:2006.03788 [hep-ph].

[22] K. S. Myint, Y. Akaishi, M. Hassanvand, and T. Yamazaki, Single-pole Nature of the Detectable Lambda(1405), PTEP **2018**, 073D01 (2018), arXiv:1804.08240 [nucl-th].

[23] K. Miyahara, T. Hyodo, and W. Weise, Construction of a local $\bar{K}N - \pi\Sigma - \pi\Lambda$ potential and composition of the $\Lambda(1405)$, Phys. Rev. C **98**, 025201 (2018), arXiv:1804.08269 [nucl-th].

[24] K. Miyahara and T. Hyodo, Theoretical study of $\Lambda(1405)$ resonance in $\Xi_b^0 \to D^0(\pi\Sigma)$ decay, Phys. Rev. C **98**, 025202 (2018), arXiv:1803.05572 [nucl-th].

[25] K. Azizi, Y. Sarac, and H. Sundu, Investigation of $\Lambda(1405)$ as a molecular pentaquark state, (2023), arXiv:2306.07393 [hep-ph].

[26] J.-M. Xie, J.-X. Lu, L.-S. Geng, and B.-S. Zou, Two-pole structures demystified: chiral dynamics at work, (unpublished) (2023), arXiv:2307.11631 [hep-ph].

[27] J.-X. Lu, L.-S. Geng, M. Doering, and M. Mai, Cross-Channel Constraints on Resonant Antikaon-Nucleon Scattering, Phys. Rev. Lett. **130**, 071902 (2023), arXiv:2209.02471 [hep-ph].

[28] R. Aaij *et al.* (LHCb), Test of lepton universality with $B^0 \to K^{*0}\ell^+\ell^-$ decays, JHEP **08**, 055, arXiv:1705.05802 [hep-ex].

[29] P. Gubler, T. T. Takahashi, and M. Oka, Flavor structure of Λ baryons from lattice QCD: From strange to charm quarks, Phys. Rev. D **94**, 114518 (2016), arXiv:1609.01889 [hep-lat].

[30] B. J. Menadue, W. Kamleh, D. B. Leinweber, and M. S. Mahbub, Isolating the $\Lambda(1405)$ in Lattice QCD, Phys. Rev. Lett. **108**, 112001 (2012), arXiv:1109.6716 [hep-lat].

[31] G. P. Engel, C. B. Lang, and A. Schäfer (BGR (Bern-Graz-Regensburg)), Low-lying Λ baryons from the lattice, Phys. Rev. D **87**, 034502 (2013), arXiv:1212.2032 [hep-lat].

[32] G. P. Engel, C. B. Lang, D. Mohler, and A. Schäfer (BGR), QCD with Two Light Dynamical Chirally Improved Quarks: Baryons, Phys. Rev. D **87**, 074504 (2013), arXiv:1301.4318 [hep-lat].

[33] Y. Nemoto, N. Nakajima, H. Matsufuru, and H. Suganuma, Negative parity baryons in quenched anisotropic lattice QCD, Phys. Rev. D **68**, 094505 (2003), arXiv:hep-lat/0302013.

[34] T. Burch, C. Gattringer, L. Y. Glozman, C. Hagen, D. Hierl, C. B. Lang, and A. Schäfer, Excited hadrons on the lattice: Baryons, Phys. Rev. D **74**, 014504 (2006), arXiv:hep-lat/0604019.

[35] T. T. Takahashi and M. Oka, Low-lying Lambda Baryons with spin 1/2 in Two-flavor Lattice QCD, Phys. Rev. D **81**, 034505 (2010), arXiv:0910.0686 [hep-lat].

[36] S. Meinel and G. Rendon, Charm-baryon semileptonic decays and the strange Λ^* resonances: New insights from lattice QCD, Phys. Rev. D **105**, L051505 (2022), arXiv:2107.13084 [hep-ph].

[37] J. M. M. Hall, W. Kamleh, D. B. Leinweber, B. J. Menadue, B. J. Owen, A. W. Thomas, and R. D. Young, Lattice QCD Evidence that the $\Lambda(1405)$ Resonance is

an Antikaon-Nucleon Molecule, Phys. Rev. Lett. **114**, 132002 (2015), arXiv:1411.3402 [hep-lat].

[38] C. Lang and V. Verduci, Scattering in the πN negative parity channel in lattice QCD, Phys.Rev. **D87**, 054502 (2013), arXiv:1212.5055.

[39] D. Mohler, S. Prelovsek, and R. M. Woloshyn, $D\pi$ scattering and D meson resonances from lattice QCD, Phys. Rev. **D87**, 034501 (2013), arXiv:1208.4059 [hep-lat].

[40] D. J. Wilson, R. A. Briceno, J. J. Dudek, R. G. Edwards, and C. E. Thomas, Coupled $\pi\pi, K\bar{K}$ scattering in P-wave and the ρ resonance from lattice QCD, Phys. Rev. **D92**, 094502 (2015), arXiv:1507.02599 [hep-ph].

[41] M. Fukugita, Y. Kuramashi, M. Okawa, H. Mino, and A. Ukawa, Hadron scattering lengths in lattice QCD, Phys. Rev. **D52**, 3003 (1995), arXiv:hep-lat/9501024 [hep-lat].

[42] C. W. Bernard and M. F. L. Golterman, Finite volume two pion energies and scattering in the quenched approximation, Phys. Rev. D **53**, 476 (1996), arXiv:hep-lat/9507004.

[43] W. Detmold and A. Nicholson, Low energy scattering phase shifts for meson-baryon systems, Phys. Rev. **D93**, 114511 (2016), arXiv:1511.02275 [hep-lat].

[44] A. Torok, S. R. Beane, W. Detmold, T. C. Luu, K. Orginos, A. Parreno, M. J. Savage, and A. Walker-Loud, Meson-Baryon Scattering Lengths from Mixed-Action Lattice QCD, Phys. Rev. **D81**, 074506 (2010), arXiv:0907.1913 [hep-lat].

[45] G.-W. Meng, C. Miao, X.-N. Du, and C. Liu, Lattice study on kaon nucleon scattering length in the $I = 1$ channel, Int. J. Mod. Phys. A **19**, 4401 (2004), arXiv:hep-lat/0309048.

[46] J. Bulava, A. D. Hanlon, B. Hörz, C. Morningstar, A. Nicholson, F. Romero-López, S. Skinner, P. Vranas, and A. Walker-Loud, Elastic nucleon-pion scattering at $m_\pi = 200$ MeV from lattice QCD, Nucl. Phys. B **987**, 116105 (2023), arXiv:2208.03867 [hep-lat].

[47] G. Moir, M. Peardon, S. M. Ryan, C. E. Thomas, and D. J. Wilson, Coupled-Channel $D\pi$, $D\eta$ and $D_s\bar{K}$ Scattering from Lattice QCD, JHEP **10**, 011, arXiv:1607.07093 [hep-lat].

[48] R. A. Briceno, J. J. Dudek, R. G. Edwards, and D. J. Wilson, Isoscalar $\pi\pi, K\overline{K}, \eta\eta$ scattering and the σ, f_0, f_2 mesons from QCD, Phys. Rev. **D97**, 054513 (2018), arXiv:1708.06667 [hep-lat].

[49] A. J. Woss, C. E. Thomas, J. J. Dudek, R. G. Edwards, and D. J. Wilson, b_1 resonance in coupled $\pi\omega$, $\pi\phi$ scattering from lattice QCD, Phys. Rev. D **100**, 054506 (2019), arXiv:1904.04136 [hep-lat].

[50] J. J. Dudek, R. G. Edwards, C. E. Thomas, and D. J. Wilson (Hadron Spectrum), Resonances in coupled $\pi K - \eta K$ scattering from quantum chromodynamics, Phys. Rev. Lett. **113**, 182001 (2014), arXiv:1406.4158 [hep-ph].

[51] S. Prelovsek, S. Collins, D. Mohler, M. Padmanath, and S. Piemonte, Charmonium-like resonances with $J^{PC} = 0^{++}$, 2^{++} in coupled $D\overline{D}$, $D_s\overline{D}_s$ scattering on the lattice, JHEP **06**, 035, arXiv:2011.02542 [hep-lat].

[52] J. Bulava, B. Cid-Mora, A. D. Hanlon, B. Hörz, D. Mohler, C. Morningstar, J. Moscoso, A. Nicholson, F. Romero-López, S. Skinner, and A. Walker-Loud, The two-pole nature of the $\Lambda(1405)$ from lattice QCD, (unpublished) (2023), arXiv:2307.10413 [hep-lat].

[53] M. Bruno *et al.*, Simulation of QCD with $N_f = 2 + 1$ flavors of non-perturbatively improved Wilson fermions, JHEP **02**, 043, arXiv:1411.3982 [hep-lat].

[54] M. Luscher and P. Weisz, On-Shell Improved Lattice Gauge Theories, Commun. Math. Phys. **97**, 59 (1985), [Erratum: Commun. Math. Phys.98,433(1985)].

[55] J. Bulava and S. Schaefer, Improvement of $N_f = 3$ lattice QCD with Wilson fermions and tree-level improved gauge action, Nucl. Phys. **B874**, 188 (2013), arXiv:1304.7093 [hep-lat].

[56] M. Lüscher and S. Schaefer, Lattice QCD without topology barriers, JHEP **07**, 036, arXiv:1105.4749 [hep-lat].

[57] M. A. Clark and A. D. Kennedy, Accelerating dynamical fermion computations using the rational hybrid Monte Carlo (RHMC) algorithm with multiple pseudofermion fields, Phys. Rev. Lett. **98**, 051601 (2007), arXiv:hep-lat/0608015 [hep-lat].

[58] D. Mohler and S. Schaefer, Remarks on strange-quark simulations with Wilson fermions, Phys. Rev. D **102**, 074506 (2020), arXiv:2003.13359 [hep-lat].

[59] M. Lüscher and F. Palombi, Fluctuations and reweighting of the quark determinant on large lattices, *Proceedings, 26th International Symposium on Lattice field theory (Lattice 2008): Williamsburg, USA, July 14-19, 2008*, PoS **LATTICE2008**, 049 (2008), arXiv:0810.0946 [hep-lat].

[60] S. Kuberski, Low-mode deflation for twisted-mass and RHMC reweighting in lattice QCD, (2023), arXiv:2306.02385 [hep-lat].

[61] M. Bruno, T. Korzec, and S. Schaefer, Setting the scale for the CLS $2 + 1$ flavor ensembles, Phys. Rev. **D95**, 074504 (2017), arXiv:1608.08900 [hep-lat].

[62] B. Strassberger *et al.*, Scale setting for CLS 2+1 simulations, PoS **LATTICE2021**, 135 (2022), arXiv:2112.06696 [hep-lat].

[63] C. Morningstar, J. Bulava, B. Fahy, J. Foley, Y. Jhang, *et al.*, Extended hadron and two-hadron operators of definite momentum for spectrum calculations in lattice QCD, Phys.Rev. **D88**, 014511 (2013), arXiv:1303.6816 [hep-lat].

[64] C. Morningstar, J. Bulava, J. Foley, K. J. Juge, D. Lenkner, M. Peardon, and C. H. Wong, Improved stochastic estimation of quark propagation with Laplacian Heaviside smearing in lattice QCD, Phys. Rev. **D83**, 114505 (2011), arXiv:1104.3870 [hep-lat].

[65] M. Peardon, J. Bulava, J. Foley, C. Morningstar, J. Dudek, R. G. Edwards, B. Joo, H.-W. Lin, D. G. Richards, and K. J. Juge (Hadron Spectrum), A Novel quark-field creation operator construction for hadronic physics in lattice QCD, Phys. Rev. **D80**, 054506 (2009), arXiv:0905.2160 [hep-lat].

[66] C. Morningstar and M. J. Peardon, Analytic smearing of SU(3) link variables in lattice QCD, Phys. Rev. **D69**, 054501 (2004), arXiv:hep-lat/0311018 [hep-lat].

[67] B. Hörz and A. Hanlon, Two- and three-pion finite-volume spectra at maximal isospin from lattice QCD, Phys. Rev. Lett. **123**, 142002 (2019), arXiv:1905.04277 [hep-lat].

[68] G. S. Bali, V. Braun, S. Collins, A. Schäfer, and J. Simeth (RQCD), Masses and decay constants of the η and η' mesons from lattice QCD, JHEP **08**, 137, arXiv:2106.05398 [hep-lat].

[69] M. Cè *et al.*, Window observable for the hadronic vacuum polarization contribution to the muon g-2 from lattice QCD, Phys. Rev. D **106**, 114502 (2022), arXiv:2206.06582 [hep-lat].

[70] C. Michael and I. Teasdale, Extracting Glueball Masses From Lattice QCD, Nucl. Phys. **B215**, 433 (1983).

[71] M. Luscher and U. Wolff, How to Calculate the Elastic Scattering Matrix in Two-dimensional Quantum Field Theories by Numerical Simulation, Nucl. Phys. **B339**, 222 (1990).

[72] B. Blossier, M. Della Morte, G. von Hippel, T. Mendes, and R. Sommer, On the generalized eigenvalue method for energies and matrix elements in lattice field theory, JHEP **04**, 094, arXiv:0902.1265 [hep-lat].

[73] S. Aoki *et al.* (CP-PACS), Lattice QCD Calculation of the rho Meson Decay Width, Phys. Rev. D **76**, 094506 (2007), arXiv:0708.3705 [hep-lat].

[74] M. Lüscher, Two particle states on a torus and their relation to the scattering matrix, Nucl. Phys. **B354**, 531 (1991).

[75] K. Rummukainen and S. A. Gottlieb, Resonance scattering phase shifts on a nonrest frame lattice, Nucl. Phys. **B450**, 397 (1995), arXiv:hep-lat/9503028 [hep-lat].

[76] C. H. Kim, C. T. Sachrajda, and S. R. Sharpe, Finite-volume effects for two-hadron states in moving frames, Nucl. Phys. **B727**, 218 (2005), arXiv:hep-lat/0507006 [hep-lat].

[77] S. He, X. Feng, and C. Liu, Two particle states and the S-matrix elements in multi-channel scattering, JHEP **07**, 011, arXiv:hep-lat/0504019 [hep-lat].

[78] V. Bernard, M. Lage, U. G. Meissner, and A. Rusetsky, Scalar mesons in a finite volume, JHEP **01**, 019, arXiv:1010.6018 [hep-lat].

[79] M. Göckeler, R. Horsley, M. Lage, U. G. Meißner, P. E. L. Rakow, A. Rusetsky, G. Schierholz, and J. M. Zanotti, Scattering phases for meson and baryon resonances on general moving-frame lattices, Phys. Rev. **D86**, 094513 (2012), arXiv:1206.4141 [hep-lat].

[80] R. A. Briceno and Z. Davoudi, Moving multichannel systems in a finite volume with application to proton-proton fusion, Phys. Rev. **D88**, 094507 (2013), arXiv:1204.1110 [hep-lat].

[81] R. A. Briceno, Two-particle multichannel systems in a finite volume with arbitrary spin, Phys. Rev. **D89**, 074507 (2014), arXiv:1401.3312 [hep-lat].

[82] C. Morningstar, J. Bulava, B. Singha, R. Brett, J. Fallica, A. Hanlon, and B. Hörz, Estimating the two-particle K-matrix for multiple partial waves and decay channels from finite-volume energies, Nucl. Phys. **B924**, 477 (2017), arXiv:1707.05817 [hep-lat].

[83] G. Källén, *Elementary Particle Physics* (Addison-Wesley, 1964).

[84] J. M. Blatt and L. C. Biedenharn, Neutron-Proton Scattering with Spin-Orbit Coupling. 1. General Expressions, Phys. Rev. **86**, 399 (1952).

[85] P. Guo, J. Dudek, R. Edwards, and A. P. Szczepaniak, Coupled-channel scattering on a torus, Phys. Rev. D **88**, 014501 (2013), arXiv:1211.0929 [hep-lat].

[86] W. I. Jay and E. T. Neil, Bayesian model averaging for analysis of lattice field theory results, Phys. Rev. D **103**, 114502 (2021), arXiv:2008.01069 [stat.ME].

[87] J. D. Hunter, Matplotlib: A 2d graphics environment, Computing in Science & Engineering **9**, 90 (2007).

[88] J. R. Green, A. D. Hanlon, P. M. Junnarkar, and H. Wittig, Weakly Bound H Dibaryon from SU(3)-Flavor-Symmetric QCD, Phys. Rev. Lett. **127**, 242003 (2021), arXiv:2103.01054 [hep-lat].

[89] Z. T. Draper, M. T. Hansen, F. Romero-López, and S. R. Sharpe, Three relativistic neutrons in a finite volume, (2023), arXiv:2303.10219 [hep-lat].

[90] D. Stanzione, J. West, R. Evans, T. Minyard, O. Ghattas, and D. Panda, Frontera: The evolution of leadership computing at the national science foundation, in *Proceedings of Practice and Experience in Advanced Research Computing (PEARC '20)* (2020).

[91] C. R. Harris, K. J. Millman, S. J. Van Der Walt, R. Gommers, P. Virtanen, D. Cournapeau, E. Wieser, J. Taylor, S. Berg, N. J. Smith, *et al.*, Array programming with numpy, Nature **585**, 357 (2020).

[92] R. G. Edwards and B. Joo (SciDAC), The Chroma software system for lattice QCD, Nucl. Phys. Proc. Suppl. **140**, 832 (2005).